Optics & Laser Technology 161 (2023) 109133

Contents lists available at ScienceDirect

Optics and Laser Technology

journal homepage: www.elsevier.com/locate/optlastec

Research Note

Increasing the build rate of high-strength aluminium alloys produced by laser powder bed fusion

Giuseppe Del Guercio, Marco Simonelli *

Centre for Additive Manufacturing, Faculty of Engineering, University of Nottingham, Nottingham NG8 1BB, United Kingdom

ARTICLE INFO

Keywords:
Laser powder bed fusion
Aluminium
Build rate
Productivity
Porosity
Hot cracking

ABSTRACT

Aluminium alloys from the 2xxx series represent important structural materials due to their optimal combination of strength and corrosion resistance. However, their production by means of laser powder bed fusion (PBF-LB/M) is hampered by the presence of detrimental pores and hot cracks. These defects can be mitigated with appropriate process parameters investigations, often at the expense of the build rate.

In this study, a combination of modelling and experimental work is adopted to predict the consolidation behaviour of AA2024, a well-known high-strength Al alloy, in regimes characterised by a progressive increase of build rate. The melt pool geometries are predicted as a function of various process parameters using the Rosenthal solution and variable values of absorptivity. This leads to a facile production of near-full dense crack-free parts at an increasing build rate. The analysis of the specimens produced with such processing parameters reveals that the microstructural features and mechanical properties of AA2024 are largely preserved when build rate is increased.

Our approach can be easily implemented in standard PBF-LB/M systems as it does not rely on machine adaptations. Therefore, our new proposed approach might result in a practical solution to increase the productivity of other high-strength Al-alloys in industrial settings.

1. Introduction

Aluminium (Al) alloys of the 2xxx series are important engineering materials for the aerospace and automotive sectors given a balance of moderate to high strength and good corrosion resistance [1]. In recent years the demand for moderate to high strength Al parts fabricated by additive manufacturing (AM) has increased significantly given the design freedom capabilities enabled by these digital manufacturing technologies [2]. The production of structural aluminium components by AM and specifically laser powder bed fusion (PBF-LB/M) has however yet to achieve its transformative potential for digitalised manufacturing. A major remaining technical challenge is to eliminate the formation of defects such as pores and cracks during processing as these are detrimental to part properties [3]. In addition, while AM is typically economical for small batch production, long build times limit the number of parts for which PBF-LB/M can be considered similarly or more productive than traditional manufacturing processes [4].

Cracking of aluminium alloys for use in structural engineering applications, including delamination and hot cracking phenomena [5], has proven to be particularly difficult to overcome. Delamination issues arise from the detrimental development of residual thermal stresses which lead to the presence of cracks aligned perpendicular to the building direction [5]. On the other hand, hot cracks form during the liquid-to-solid transition due to the development of detrimental strain rates and thermal gradients [6]. Although both of these phenomena may occur during PBF-LB/M fabrication, high-strength Al-alloys are well known to suffer predominantly by the formation of hot cracks [7] and therefore this investigation focuses on such defects.

Currently-two main approaches are adopted to mitigate the formation of hot cracks in Al-alloys processed by PBF-LB/M. The most common method is represented by grain inoculation, a well-consolidated technique in casting in which the addition of selected compounds to the base material promotes the presence of a refined microstructure thought to be advantageous to mitigate hot crack formation [8]. Despite its potential, this method is paired with high material costs and difficulties in implementation in large scale industrial settings. Additionally, inoculants alter the base alloy's properties resulting in further required qualifications that limit their industrial application.

* Corresponding author.
E-mail address: marco.simonelli@nottingham.ac.uk (M. Simonelli).

https://doi.org/10.1016/j.optlastec.2023.109133
Received 25 November 2022; Received in revised form 22 December 2022; Accepted 3 January 2023
Available online 9 January 2023

There is substantial research showing that crack intensity can be affected by changing the processing regimes used in PBF-LB/M. Successful examples of strategies that reduce cracking are the use of pre-heated substrates [9] and/or regimes characterised by low laser scan speed [10–12] which are thought to reduce the cooling rates during solidification of the melt pool and in turn its sensitivity to cracking [13,14]. The use of pre-heated substrates is not readily transferrable across different PBF-LB/M setups as not all machines have similar pre-heating capabilities. In addition, this can lead to pronounced segregation of selective alloying elements in the interdendritic region as well as gas porosity due to selective evaporation [15]. Similarly, processing regimes based on low laser scan speed, although capable to produce crack-free parts, are often non-optimised for productivity.

In these regards, there remains a need to understand how cracking during PBF-LB/M can be suppressed whilst optimising build rates. The aim of this present study is to investigate the sensitivity of cracking to the main process parameters in PBF-LB/M. For this, we carry out a combined modelling and experimental work to identify a pathway that enables the production of defect free AA2024 at different build rates.

2. Materials and methods

AA2024 powder was procured from TLS Technik AG GmbH. The feedstock was characterised by a near-spherical morphology and the size analysis, conducted using a Mastersizer 3000 (Malvern Panalytical), showed values of D10, D50 and D90 of 29.5, 42.1 and 59.6 μm, respectively. The composition of the powders was investigated via Inductively Coupled Plasma Optical Emission Spectroscopy (ICP-OES) and the results are listed in Table 1.

Cubic samples of 10 mm edge were produced using a Renishaw AM400 featuring a 400 W ytterbium fibre laser and a Reduced Build Volume (RBV) set up. During processing, the build chamber was held under an Ar atmosphere to minimise oxidation with an oxygen content below 400 ppm. A meander scan strategy, where the direction of laser tracks was rotated by 67° at each layer, was adopted. As largely reported [13,16,17], hot crack formation results to be strongly affected by the scan speed with low values limiting the presence of such detrimental defects. Starting from the values reported in literature [13,16,17], a few samples were printed to investigate the applicability of these low scan speed laser regimes on the Renishaw AM400 system. As a result, the specimens investigated in the present work were produced using a laser scan speed v of 0.107 m/s (point distance of 15 μm, exposure time of 120 μs and an inter-pulse delay of 20 μs), which proved to be effective to fabricate crack-free parts. The parameters that were investigated with the aim to increase build rate are summarised in Table 2. These regimes were paired with a wide range of volumetric energy density (VED), which assumed values between 207.68 and 778.82 J/mm^3. Low P and both high Δz and h_d were characterised with the lower VED; on the other hand, high P and low Δz and h_d resulted in samples produced with the higher VED in the cited range.

After PBF-LB/M processing, all the samples were cross-sectioned parallel to the building direction and subsequently mounted, ground, and polished with a final finish of colloidal silica. A Nikon Eclipse LV100ND microscope was adopted to collect optical micrographs which were subsequently analysed to measure the samples' relative density following the procedure illustrated in one of the authors previous publications [13]. A JEOL 7100 FEG-SEM was used to obtain backscattered micrographs of representative samples. The average cell size was measured at the melt pool boundaries considering 10 adjacent cells. The phases present in these specimens were identified via X-ray diffraction (XRD) which was conducted with a Bruker D8 Advance Da Vinci equipped with a Lynxeye 1D detector. Data were acquired with a step size of 0.02° and a step time of 4 s between 2θ values of 20° and 90°. The hardness of the produced samples was measured using a Wilson VH3100 (Buehler ltd.). In total, 20 indents per sample were performed using a 10 s dwell time and measuring their diagonals at the same magnification of 50x. They were located in the core of the vertical plane of the samples at random positions. In order to minimise lack-of-fusion defects we have adopted a melt pool geometrical model as described by Tang et al. [18]. Following this approach, complete melt pool overlap is guaranteed in the event Equation (1) holds:

Table 1
Chemical composition of the AA2024 alloy investigated in the present work.

Cu	Mg	Si	Mn	Fe	Al
4.57	1.34	0.36	0.98	0.12	Bal.

Table 2
List of process parameters investigated in this work.

Parameters	Values
Power P [W]	200, 220, 240, 260, 280, 300
Layer thickness Δz [μm]	30, 35, 40, 45, 50
Hatch distance h_d [μm]	120, 130, 140, 150, 160, 170, 180

$$\left(\frac{h_d}{w}\right)^2 + \left(\frac{\Delta z}{d}\right)^2 \leq 1 \tag{1}$$

where w and d represent the melt pool's width and depth, respectively. These were evaluated approximating the temperature distribution T with the Rosenthal solution [19]:

$$T = T_0 + \frac{AP}{2\pi k\sqrt{x^2+y^2+z^2}}\exp\left[-\frac{v\left(x+\sqrt{x^2+y^2+z^2}\right)\rho c_p}{2k}\right] \tag{2}$$

where T_0 can be approximated with the platform temperature (300 K), k represents the thermal conductivity (193 W/(m K) [1]), ρ is the density of the alloy (2780 kg/m^3), c_p its specific heat (875 J/(kg K) [1]), x, y and z are the spatial coordinates and A represents the powder absorptivity. This approach assumes that the melt pools are predominantly produced in conduction mode (no evaporation or keyholing) and that thermo-physical properties are constant with temperature. As the different laser powers investigated in this work produce different melt pool geometries, different values of absorptivity need to be considered. The corresponding absorptivity values were determined using an in-situ laser micro-calorimeter [20] and are shown in Fig. 1. The solidus and liquidus temperatures of AA2024, needed to evaluate the melt pool's dimensions, were computed with the CALPHAD approach using Thermo-Calc™ 2021b [21], the TCAL6 database [22] and the composition listed in Table 1 as input material.

The build rate $\dot{V}$ was calculated using the model proposed by Buchbinder et al. [23]:

$$\dot{V} = \Delta z \bullet h_d \bullet v \tag{3}$$

Despite not considering the time associated to laser jumps and powder spreading, Equation (3) is able to capture the effects of the main parameters affecting PBF-LB/M productivity, especially considering simple geometries such as those investigated in the present work [24].

3. Results

In order to minimise the formation of lack-of-fusion porosity we use the modelling approach described in Section 2. Fig. 2(a) shows the relationship between the predicted melt pool size and the nominal values of layer thickness and hatch distance. It is widely known that to avoid the formation of lack-of-fusion it is necessary to satisfy the condition posed by Equation (1) [18]. Graphically, the various processing regimes are represented by distinct points in Fig. 2(a), where points comprised within the area of the graph shaded in green are considered adequate regimes against the formation of lack-of-fusion defects. Fig. 2 (b-g) depicts optical micrographs of the typical microstructure of

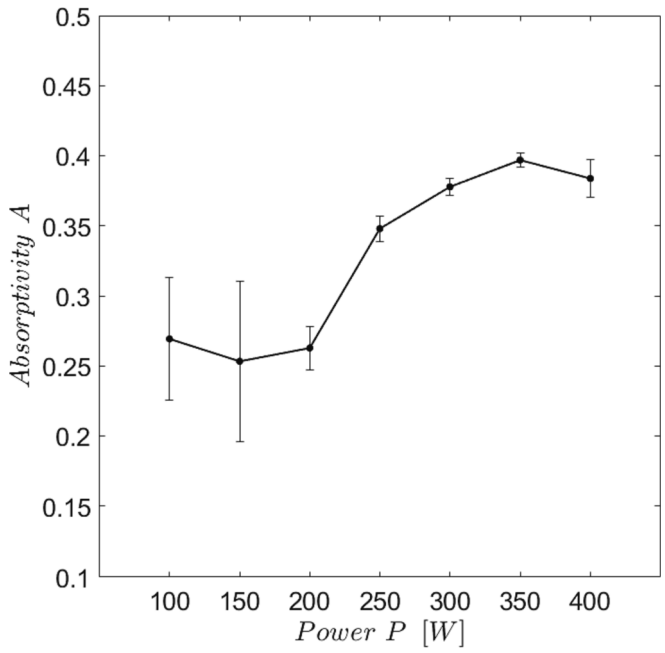

Fig. 1. Powder absorptivity trend as a function of laser power. At laser powers below 200 W scan tracks were discontinuous and therefore the absorptivity showed great variability. On the other hand, at laser powers exceeding 300 W tracks were found to be characterised by deep V-shaped melt pools, typical of the keyhole melting mode. Powers between 200 and 300 W (adopted in the present study) were found to be characterised by stable melt pools and therefore these regimes are thought to be melted predominantly in conduction mode.

samples produced with 260 W but different h_d and Δz. It can be observed that these specimens, as predicted in Fig. 2(a), are characterised by the absence of lack-of-fusion pores with the occasional presence of minimal gas porosity. Even more importantly, the absence of both delamination and hot cracks is observed resulting in near-full dense parts. Similar results have been observed in all other processing regimes investigated in the present work. The graph in Fig. 2(a) shows that the specimen depicted in Fig. 2(b) is extremely conservative and that the fusion zone created by newly deposited layers extend significantly in the prior layers as well as a large overlap between adjacent melt tracks exists. As all process parameters except layer thickness are kept constant, it is assumed that the increase in layer thickness (from (b) to (c)) will cause a reduction in layer overlap along the build direction. Similarly, the increase in hatch distance (from (d) to (g)) will cause a reduction in transverse melt pool overlap. Nevertheless, as predicted and experimentally observed in Fig. 2, these regimes result to be within an acceptable processing map paired with near-full dense defects-free parts.

Fig. 3 is a contour plot that shows how build rate varies with respect to layer thickness and hatch spacing. It can be observed that, within the process parameters range here investigated, to achieve maximum build rate both the layer thickness and the hatch spacing need to be increased. It can also be noticed that the contour lines have a relatively low gradient with respect to the h_d, that is build rate is predominantly influence by Δz. We therefore compare in detail three build regimes within the range of parameters investigated to establish a pathway to fabricate good quality AA2024 parts. These regimes are labelled in Fig. 3 and correspond to Fig. 2(b) (point A), 2(d) (point B) and 2(g) (point C). Point A, considered as reference specimen, represents the sample fabricated with a layer thickness of 30 μm which is the default Δz used to process "difficult-to-weld" materials [13,14,25]. This is then compared to point B, a material produced by increasing the layer thickness to 50 μm, leading to an increase in build rate of approx. 50 %. Finally, we investigate an additional point in the processing map (point C), where the hatch spacing is increased from 120 to 180 μm to achieve a further 50 % increment in build rate.

Fig. 4(a-c) depicts a comparison of the experimental (left half) and predicted (right half) melt pool traces of samples A, B and C, respectively. As can be observed, the computation of the melt pool traces with the methodology discussed in Section 2 finds great agreement with the experimental findings. The first striking difference in the microstructure of the specimens is a different prevalence of the fusion boundaries in the micrographs. Although these are projections of the melt pool traces in 2D planes, it is possible to observe that specimen A is characterised by a large number of melt pool boundaries, while these become progressively less obvious in specimen B and C. This is justified considering that at every laser pass, the laser creates a melt pool and a heat affected zone (delimited by fusion boundaries) where the solidification structure appears coarser, giving rise to the boundaries observed in the micrographs. The larger melt pool overlap in point A would cause an increase in the number of these features in the micrographs. The underlying Al-FCC grain structure also appears to be affected by the processing regime. It is observed that point A is characterised by grain predominantly elongated towards the build direction (Fig. 4(a)). This appears less obvious in the point B and then C where stray grain morphologies also develop (Fig. 4(c)).

Consistently to that reported in one of our previous investigations [15], the phase constituents found in the specimens appear to be Al-FCC matrix (grey contrast in the micrographs) with Al_2Cu (θ-phase) and

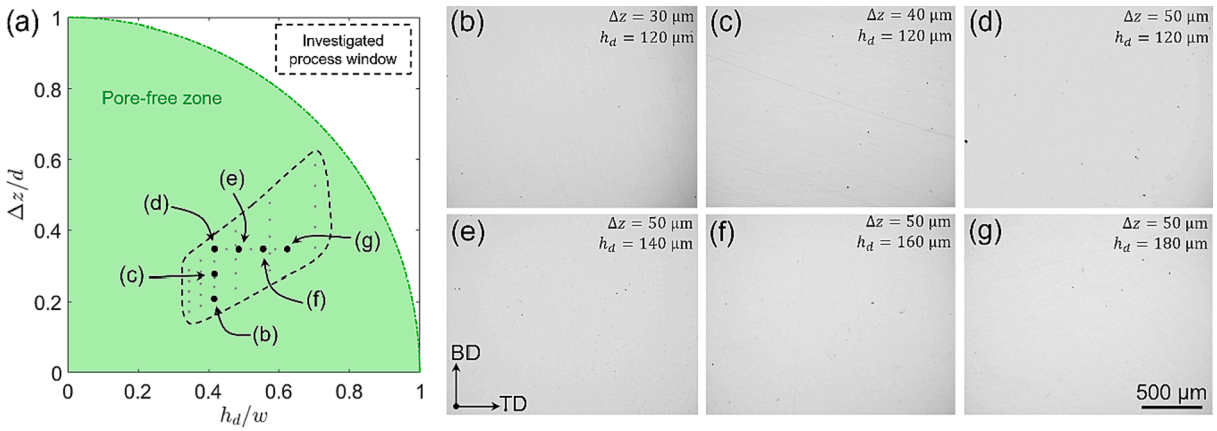

Fig. 2. (a) Graphical prediction of processing regimes where lack-of-fusion defects are avoided. All the processing regimes investigated in the present work are expected to be characterised by optimal overlap in both the transverse (TD) and building direction (BD) resulting in defects-free parts. (b-g) Optical micrographs of selected samples printed with a $P = 260$W and a progressive increase of (b-d) layer thickness and (d-g) hatch distance.

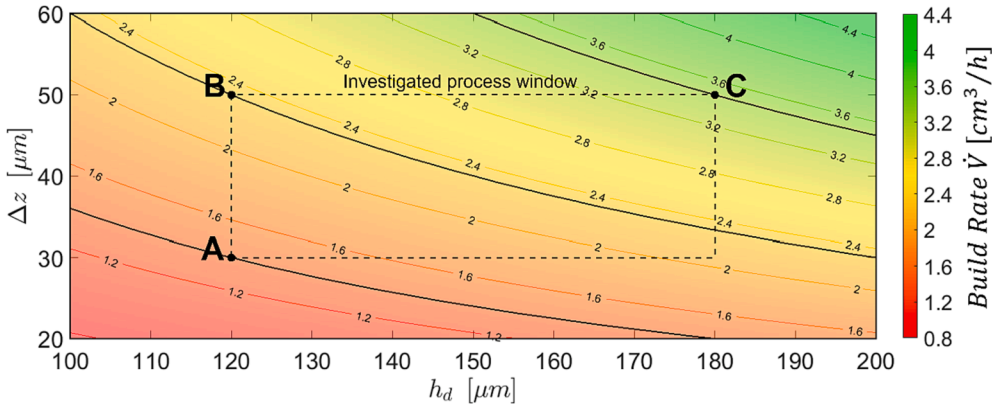

Fig. 3. Contour plot of the build rate with respect to hatch distance and layer thickness. Within the processing window (dashed box), three regimes (A, B and C) are considered to investigate the evolution of the microstructural features and hardness as a function of the build rate.

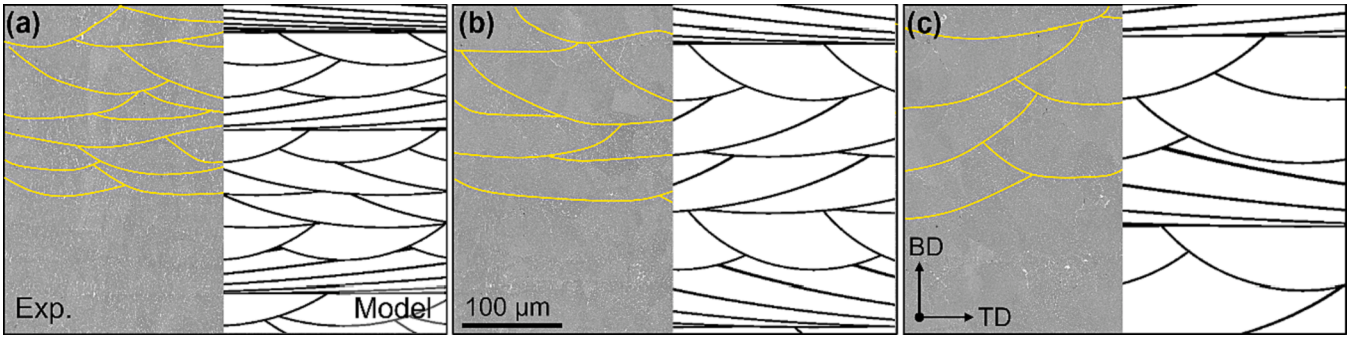

Fig. 4. Melt pool overlap comparison between the experimental samples (BSE micrographs – left, fusion boundaries highlighted in yellow) and the predicted traces obtained by implementing the Rosenthal solution corrected by experimentally measured absorptivity values (right, in black). (a), (b) and (c) depict specimens A, B and C, respectively. (For interpretation of the references to colour in this figure legend, the reader is referred to the web version of this article.)

Al_3Mg_2 (β-phase) appearing at the grain and dendritic boundaries (bright contrast in the micrographs). Additionally, it is found that the typical solidification structure has similar size across the specimens investigated (Fig. 5(a)). The values of hardness measured for the considered samples are reported in Fig. 5(b). It can be observed that the hardness of the specimens is not significantly different. These values well agree with previous experimental findings reported in the literature for both PBF-LB/M processed specimens [12,17] and traditionally wrought products [1].

4. Discussion

This research shows a pathway for the production defect free high-strength aluminium alloys. It is shown that thicker layers can increase throughput significantly, with no penalty to microstructure development or mechanical performance. This is valid when the melt pool can be described by the conduction mode melting and their stability does not vary with increased target penetration depth. For Al alloys, this is the case when medium laser powders are used (in the range between 200 and 300 W in the present investigation) and keyholing is largely avoided. This is reflected in the measured values of absorptivity (Fig. 1) which show the plateau keyhole regime at powers greater than 300 W

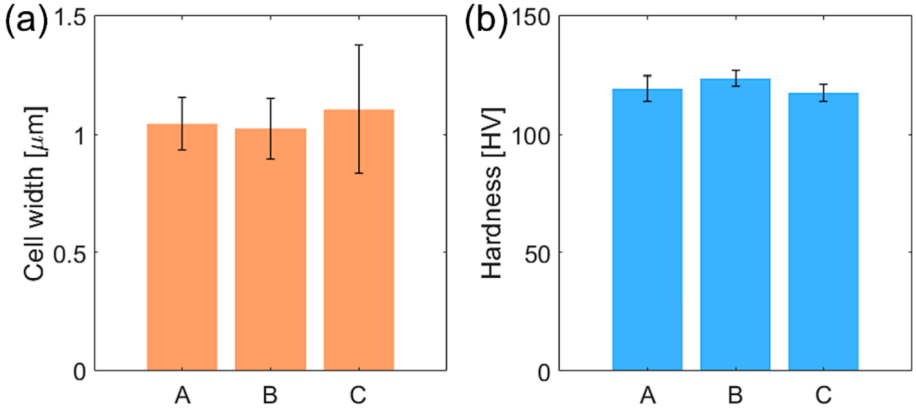

Fig. 5. (a) Average solidification cell widths and (b) hardness values measured for specimens A, B and C.

(never exceeded in the present investigation).

It is noteworthy that no cracks are observed in any of the investigated samples. This is explained by the fact that the solidification dynamics which promote the formation hot crack are mainly influenced by the energy input (chiefly, the laser power and laser scan speed) and the platform temperature [26]. Since these process parameters are largely unchanged, the driving force for initiation of hot cracks is similar in all the investigated specimens and below the threshold for crack formation in AA2024. The findings clearly show that layer thickness and hatch spacing have no significant influence in the formation of hot cracks, at least in the range of processing regimes investigated in this study.

It is expected that the use of thicker layers would invoke penalty in dimensional accuracy and surface finish due to coarser slicing and inevitable staircase effect [27]. This is subject of ongoing investigations. However, it is noted that most structural applications of AA2024 will require some post-processing machining steps and therefore at least a relative increase in surface finish this does not appear to be of crucial importance.

5. Conclusions

This research investigates the consolidation behaviour of a high-strength aluminium alloy (AA2024) in processing regimes characterised by high build rates. It is found that the formation microstructural defects such as pores and cracks can be suppressed by using a thermal model based on the Rosenthal analytical solution of heat transfer of a moving point source. The main conclusions are:

1. The adoption of variable absorptivity values as a function of power proved to compute the thermal fields with the Rosenthal solution proved to be an effective strategy to successfully predict the melt pool geometries of AA2024 processed by several PBF-LB/M regimes. This enabled the identification of processing windows associated to high build rates.
2. The build rate of AA2024 can in fact be increased by 50 % when layer thickness is increased from 30 μm (default value) to 50 μm. The build rate can be further increased by using larger hatch spacings, although this parameter has a second-order influence of the productivity.
3. Increasing layer thickness cause a change in the morphology of the grain structure as the use of thick layers encourages epitaxial growth and development of vertical columnar grains.
4. The measured hardness is consistent across the specimens investigated. Despite the larger overlap caused by the use of thin layer, larger overlap does not affect the development and the coarseness of the solidification structures (the dendrite size is not affected by layer thickness or hatch spacing).

The proposed approach can be uptaken in standard machines and it does not rely on any high-cost adaptations. Therefore, it represents a practical solution to improve the build rate of aluminium alloys in industrial settings.

Author statement

G.D.G. wrote the article with the contribution of M.S. G.D.G. implemented the modelling parts, conducted the experiments and collected the micrographs. M.S. supervised all the experiments and revised the first draft of the manuscript.

Declaration of Competing Interest

The authors declare that they have no known competing financial interests or personal relationships that could have appeared to influence the work reported in this paper.

Data availability

Data will be made available on request.

Acknowledgements

The work presented here has been made possible by funding provided through the University of Nottingham's Nottingham Research Fellowship and EPSRC grant EP/P027261/1.

References

[1] A.S.M.I.H. Committee, Properties and selection: nonferrous alloys and special-purpose materials, ASM Int. 2 (1992) 1143–1144.
[2] N.T. Aboulkhair, M. Simonelli, L. Parry, I. Ashcroft, C. Tuck, R. Hague, 3D printing of aluminium alloys: additive manufacturing of aluminium alloys using selective laser melting, Prog. Mater Sci. 106 (2019), 100578, https://doi.org/10.1016/j.pmatsci.2019.100578.
[3] M. Seifi, M. Gorelik, J. Waller, N. Hrabe, N. Shamsaei, S. Daniewicz, J. J. Lewandowski, Progress towards metal additive manufacturing standardization to support qualification and certification, JOM 69 (2017) 439–455, https://doi.org/10.1007/s11837-017-2265-2.
[4] A.B. Spierings, K. Dawson, T. Heeling, P.J. Uggowitzer, R. Schäublin, F. Palm, K. Wegener, Microstructural features of Sc-and Zr-modified Al-Mg alloys processed by selective laser melting, Mater. Des. 115 (2017) 52–63.
[5] A. Martucci, A. Aversa, F. Bondioli, P. Fino, M. Lombardi, Synergic strategies to improve the PBF-LB\M processability of a cracking-sensitive alloy, Mater. Des. 224 (2022), https://doi.org/10.1016/j.matdes.2022.111396.
[6] M. Rappaz, J.M. Drezet, M. Gremaud, A new hot-tearing criterion, Metall. Mater. Trans. A 30 (1999) 449–455, https://doi.org/10.1007/s11661-999-0334-z.
[7] S.C. Altıparmak, V.A. Yardley, Z. Shi, J. Lin, Challenges in additive manufacturing of high-strength aluminium alloys and current developments in hybrid additive manufacturing, Int. J. Lightweight Mater. Manufact. 4 (2021) 246–261, https://doi.org/10.1016/j.ijlmm.2020.12.004.
[8] C.M. Gourlay, A.K. Dahle, Dilatant shear bands in solidifying metals, Nature 445 (2007) 70–73, https://doi.org/10.1038/nature05426.
[9] S.Z. Uddin, L.E. Murr, C.A. Terrazas, P. Morton, D.A. Roberson, R.B. Wicker, Processing and characterization of crack-free aluminum 6061 using high-temperature heating in laser powder bed fusion additive manufacturing, Addit. Manuf. 22 (2018) 405–415.
[10] T. Wang, Y. Wang, X. Yang, B. Chen, H. Zhu, Cracks and process control in laser powder bed fusion of Al-Zn-Mg alloy, J. Manuf. Process. 81 (2022) 571–579, https://doi.org/10.1016/j.jmapro.2022.06.066.
[11] Y. Qi, H. Zhang, X. Nie, Z. Hu, H. Zhu, X. Zeng, A high strength Al–Li alloy produced by laser powder bed fusion: densification, microstructure, and mechanical properties, Addit. Manuf. 35 (2020), 101346.
[12] H. Zhang, H. Zhu, T. Qi, Z. Hu, X. Zeng, Selective laser melting of high strength Al–Cu–Mg alloys: processing, microstructure and mechanical properties, Mater. Sci. Eng. A 656 (2016) 47–54, https://doi.org/10.1016/j.msea.2015.12.101.
[13] G. Del Guercio, D.G. McCartney, N.T. Aboulkhair, S. Robertson, R. Maclachlan, C. Tuck, M. Simonelli, Cracking behaviour of high-strength AA2024 aluminium alloy produced by Laser Powder Bed Fusion, Addit. Manuf. 54 (2022), 102776, https://doi.org/10.1016/j.addma.2022.102776.
[14] Y. Wang, X. Lin, Y. Zhao, T. Zhang, J. Fu, N. Zheng, Z. Wang, W. Huang, Cracking mechanism and its susceptibility to scanning speed during laser power bed fusion processed high-strength 2024Al alloy, Mater Charact 194 (2022), 112344, https://doi.org/10.1016/j.matchar.2022.112344.
[15] A. Bhagavatam, A. Ramakrishnan, V.S.K. Adapa, G.P. Dinda, Laser metal deposition of aluminum 7075 alloy, Int J Mater Sci Res. 1 (2018) 50–55.
[16] M. Rasch, J. Heberle, M.A. Dechet, D. Bartels, M.R. Gotterbarm, L. Klein, A. Gorunov, J. Schmidt, C. Körner, W. Peukert, M. Schmidt, Grain structure evolution of Al-Cu alloys in powder bed fusion with laser beam for excellent mechanical properties, Materials (Basel). 13 (2020), https://doi.org/10.3390/ma13010082.
[17] X. Nie, H. Zhang, H. Zhu, Z. Hu, L. Ke, X. Zeng, Analysis of processing parameters and characteristics of selective laser melted high strength Al-Cu-Mg alloys: from single tracks to cubic samples, J. Mater. Process. Technol. 256 (2018) 69–77, https://doi.org/10.1016/j.jmatprotec.2018.01.030.
[18] M. Tang, P.C. Pistorius, J.L. Beuth, Prediction of lack-of-fusion porosity for powder bed fusion, Addit. Manuf. 14 (2017) 39–48.
[19] D. Rosenthal, Mathematical theory of heat distribution during welding and cutting, Weld J. 20 (1941) 220–234.
[20] A.T. Clare, W.J. Reynolds, J.W. Murray, N.T. Aboulkhair, M. Simonelli, M. Hardy, D.M. Grant, C. Tuck, Laser calorimetry for assessment of melting behaviour in multi-walled carbon nanotube decorated aluminium by laser powder bed fusion, CIRP Ann. 69 (2020) 197–200.
[21] J.O. Andersson, T. Helander, L. Höglund, P. Shi, B. Sundman, Thermo-Calc & DICTRA, computational tools for materials science, CALPHAD: Comput. Coupling Phase Diagrams Thermochem. 26 (2002) 273–312, https://doi.org/10.1016/S0364-5916(02)00037-8.
[22] Thermo-Calc, TCAL6: TCS Al-based Allot Database, (2019). https://thermocalc.com/products/databases/aluminum-based-alloys/.

[23] D. Buchbinder, H. Schleifenbaum, S. Heidrich, W. Meiners, J. Bültmann, High power selective laser melting (HP SLM) of aluminum parts, Phys. Procedia 12 (2011) 271–278.
[24] T. Griemsmann, A. Abel, C. Hoff, J. Hermsdorf, M. Weinmann, S. Kaierle, Laser-based powder bed fusion of niobium with different build-up rates, Int. J. Adv. Manuf. Technol. 114 (2021) 305–317, https://doi.org/10.1007/s00170-021-06645-y.
[25] Q. Tan, Y. Liu, Z. Fan, J. Zhang, Y. Yin, M.-X. Zhang, Effect of processing parameters on the densification of an additively manufactured 2024 Al alloy, J. Mater. Sci. Technol. 58 (2020) 34–45.
[26] B. Mondal, T. Mukherjee, T. DebRoy, Crack free metal printing using physics informed machine learning, Acta Mater. 226 (2022), 117612, https://doi.org/10.1016/j.actamat.2021.117612.
[27] P. Das, R. Chandran, R. Samant, S. Anand, Optimum part build orientation in additive manufacturing for minimizing part errors and support structures, Procedia Manuf. 1 (2015) 343–354, https://doi.org/10.1016/j.promfg.2015.09.041.